Kinetics of chlorite dissolution at elevated temperatures and CO_2 conditions

Megan M. Smith *, Thomas J. Wolery, Susan A. Carroll

Atmospheric, Earth, and Energy Division, L-231, Lawrence Livermore National Laboratory, Livermore, CA 94550, USA

ABSTRACT

Chlorite (($Mg_{4.29}Al_{1.48}Fe_{0.10}$)($Al_{1.22}Si_{2.78}$)$O_{10}(OH)_8$) dissolution kinetics were measured under far from equilibrium conditions using a mixed-flow reactor over temperatures of 100–275 °C at pH values of 3.0–5.7 in a background solution matrix of 0.05 m NaCl. Over this temperature range, magnesium was released congruently with respect to silica. The effect of variable pCO_2 levels representative of engineered geothermal systems with CO_2 as a heat-exchanging fluid (CO_2-EGS) was explored by reacting chlorite with solutions containing a range of dissolved CO_2 concentrations (0.1–0.5 M). The dissolution rate was insensitive to $CO_{2(aq)}$ concentration, with dissolved CO_2 apparently affecting dissolution only through increased acidity. Over this range of far-from-equilibrium experimental conditions of elevated temperature, mildly acidic to moderately neutral pH, and $CO_{2(aq)}$ concentrations up to 0.5 M, Mg-rich chlorite dissolution can be described as a surface area-normalized rate equal to:

$$\text{rate} = k_{acid} \cdot \exp\left[\left(\frac{-E_{acid}}{R}\right)\cdot\left(\frac{1}{T}-\frac{1}{298\,K}\right)\right]\cdot a_{H+}^n,$$

where the apparent acid rate constant at 25 °C is $k_a = 10^{-9.91}$ mol m^{-2} s^{-1}, the reaction order n with respect to $H^+_{(aq)}$ is 0.49, and the activation energy for the acid mechanism is $E = 25.1$ kJ mol^{-1} (this value is significantly lower than previous estimates). This chlorite dissolution rate equation can be used with reaction affinity terms and kinetic laws for other minerals to estimate the impact of geochemical alteration within CO_2-enhanced geothermal system operations or other higher-temperature subsurface systems. Over a 100–275 °C temperature range, chlorite is 2–5 orders of magnitude less reactive than has been previously predicted.

© 2013 Elsevier B.V. All rights reserved.

1. Introduction

The disparities between reported kinetic rates for mineral dissolution and precipitation reactions measured in the laboratory and in field settings have been discussed previously by many others (e.g., Li et al., 2006; Maher et al., 2006). However, for many common minerals, even laboratory-obtained kinetic data are lacking, especially at elevated temperatures (see Palandri and Kharaka, 2004, and references therein). Of special concern is the lack of reliable kinetic data at temperatures above 60 °C (with the exception of recent 95 °C work on Fe- and Mg-rich biotites, Garcia et al., 2012; Hu and Jun, 2012) for many clays, micas, and other layered silicates, despite their common occurrence in subsurface reservoir systems. Because sheet silicates can be the products of secondary alteration reactions both within other mineral grains as well as in intergranular space, their reactions may strongly influence the evolution of porosity and related permeability within subsurface

systems. In order to describe and evaluate these potential reactions, additional data are required for more accurate reactive transport simulations, as has been pointed out by reviews on both engineered geothermal systems (EGS, Tester et al., 2006) and CO_2 storage (Gaus et al., 2008) technologies.

In addition to the need to predict reservoir responses within deep hydrocarbon or geothermal systems (characterized by elevated temperatures and increased abundances of alteration sheet silicates), proposed technologies which utilize injected carbon dioxide such as CO_2-enhanced geothermal systems ("CO_2-EGS," Brown, 2000) will require an understanding of the role that elevated CO_2 concentrations may play on mineral reactivity. Dissolution reactions driven by CO_2-acidified fluids could generate additional porosity and create new flowpaths, but may also trigger secondary precipitation reactions which would adversely impact reservoir permeability. The appeal of the CO_2-EGS technique is based partially on lower pumping rates (and thus lower parasitic energy losses) as a result of CO_2's higher buoyancy and lower viscosity relative to water, but the geochemical effects of CO_2 injection into high-temperature reservoirs are currently unpredictable given the available data (Pruess, 2006). Investigation of the dissolution of one framework silicate demonstrated that dissolved $CO_{2(aq)}$ played

* Corresponding author at: Lawrence Livermore National Laboratory, 7000 East Avenue, L-231, Livermore, CA 94550, USA. Tel.: +1 925 423 7970; fax: +1 925 423 4908.
E-mail addresses: megan@llnl.gov (M.M. Smith), wolery@llnl.gov (T.J. Wolery), carroll6@llnl.gov (S.A. Carroll).

only an indirect role at temperatures up to 130 °C (labradorite, Carroll and Knauss, 2005). In contrast, another sheet silicate altered extensively under wetted supercritical CO_2 conditions (biotite; Shao et al., 2011; Hu and Jun, 2012).

Chlorite minerals (sheet-structured aluminosilicates containing variable amounts of magnesium and iron) are common constituents of numerous formations and often occur as grain-coating or pore-filling growths in sedimentary sandstones, alteration products of mafic minerals in basaltic units, or as products of low-grade metamorphism of many prior assemblages. Although chlorite is commonly observed in many oil and gas reservoirs, hydrothermal systems, and some deep aquifers, little information exists concerning its reactivity under expected conditions relevant to those systems, i.e., hotter temperatures and/or anthropogenically elevated levels of CO_2. Recent modeling studies of both CO_2-EGS and geologic carbon sequestration reactions (Wolery and Carroll, 2010; Xu, 2012) included chlorite in the relevant mineral assemblages in recognition of the potential reactivity of this sheet silicate. These simulations use the kinetic formulation found in Palandri and Kharaka's (2004) kinetic rate compilation. Extrapolation of this rate equation to higher temperatures (e.g., ≥100 °C) predicts extensive chlorite dissolution as a result of high activation energy values, although a recent experimental study showed chlorite (in a natural sandstone) to be largely unreactive with CO_2-saturated reservoir brines at 120 °C, 32 MPa (Lu et al., 2012). This discrepancy highlights the motivation for extending the chlorite dissolution dataset to higher temperatures, and also for examination of the dissolution of other common minerals for which higher-temperature kinetic data are currently lacking.

The paucity of chlorite kinetic data at temperatures above 95 °C in either CO_2-free or CO_2-acidified solutions motivated us to examine chlorite dissolution rates in acid to semi-neutral solutions (both CO_2- and HCl-acidified) as a function of temperature (100–275 °C). We present a kinetic rate equation validated by new experimental data up to 275 °C for the dissolution of magnesium-rich chlorite, which can be directly implemented in existing reactive transport codes for improved simulation of water–rock interactions affecting a variety of potential scenarios (e.g., CO_2-enhanced geothermal, geologic carbon sequestration in deep reservoirs, nuclear waste disposal).

2. Experimental methods

2.1. Materials

A bulk chlorite sample was purchased from the Source Clays Repository, Purdue, Illinois, under the identifier "CCa-2," collected from El Dorado County, California, USA (Post and Plummer, 1972). The bulk specimen was crushed to pea-size and further hand-crushed and sieved to collect the 150–250 μm size fraction, but otherwise used as received. Approximately 1 g of chlorite was used per experiment. Powder X-ray diffraction (XRD) analysis was performed on the 150–250 μm size fraction, producing a diffractogram in close agreement with clinochlore patterns. Scanning electron microscopy/electron dispersive spectrometry (SEM/EDS) identified trace rutile, corroborated by electron microprobe analysis. The average chlorite composition based on microprobe analysis was $(Mg_{4.29}Al_{1.48}Fe_{0.10})$ $(Al_{1.22}Si_{2.78})O_{10}(OH)_8$, derived by distributing aluminum first in the tetrahedral site with the remainder in octahedral sites and assuming all iron as ferrous, following the recommendations and observations of Foster (1962). The surface area of the 150–250 μm size fraction was measured by N_2-BET as 5.06 ±0.38 m^2/g; samples reacted at both 100 and 275 °C showed no significant post-reaction change in measured surface area values.

The aluminum site occupancy value given above was corroborated by nuclear magnetic resonance (NMR) analysis of both unreacted and reacted samples via collection of ^{27}Al single-pulse magic angle spinning nuclear magnetic resonance spectra using a

selective 1 μs excitation pulse. ^{29}Si{^{1}H} cross-polarization magic angle spinning NMR spectra were also collected on reacted samples with a 2 s pulse delay at a 2 and 10 ms contact time and spinning rate of 3.6 kHz (referenced to tetramethylsilane) to determine silica coordination in reacted grain samples. Both unreacted and reacted sample grains were platinum coated prior to focused ion beam milling of wafers for transmission electron microscopy (TEM) and analysis using high-resolution images combined with fast Fourier transform analysis and electron diffraction. Other than the platinum-coating required for TEM analysis, reacted sample grains were used as recovered from the experimental reactors to prevent surface contamination from exposure to foreign materials or fluids.

All experiments were performed in a background solution of reagent-grade 0.05 m NaCl and distilled deionized water. Reagent-grade hydrochloric acid (HCl) was used to adjust certain solutions to specific pH levels, which are referred to in the text as "CO_2-free" experiments. CO_2-equilibrated solutions were created by heating and pressurizing prepared solutions with liquid or gaseous CO_2 in a separate static titanium reactor for at least 12 h under conditions designed to produce specific $CO_{2(aq)}$ concentrations according to Duan et al. (2006). Upstream sampling of CO_2-equilibrated solutions prior to contact with mineral solids (see Fig. 1 for port location and Section 2.3 for total inorganic carbon sampling details) confirmed that desired initial $CO_{2(aq)}$ concentrations had been attained before steady-state dissolution periods during each experiment.

2.2. Experimental reactor

Titanium mixed-flow reactors (Dove and Crerar, 1990) were used to determine chlorite dissolution kinetics over a temperature range of 100–275 °C, under both CO_2-free (control) conditions and also with $CO_{2(aq)}$ concentrations of 0.1–0.5 M (Table 1), at far-from-equilibrium conditions. The net rate (R, M L^{-2} T^{-1}) of chlorite dissolution was derived from measured changes in effluent composition ($\Delta[i]$, M_i L^{-3}; normalized using stoichiometric coefficient v_i, M_i M_{chl}^{-1}), the flowrate (FR, L^3 T^{-1}), and chlorite mass (m, M) and measured specific surface area (A, L^2 M^{-1}):

$$\text{rate} = \frac{\Delta_i \cdot FR}{v_i \cdot A \cdot m}. \tag{1}$$

An example of typical solution chemistry data displaying steady-state behavior is shown in Fig. 2. Approach to near steady-state behavior was noted as early as 36 h in some samples (~4 residence volumes) depending on sampling frequency, with data used to determine dissolution rates generally falling within the 5–8 residence volume timeframe in all cases except H1-B (100 °C experiment which demonstrated steady-state behavior after 7.8–9.5 residence volumes).

The experimental setup was similar to that described in Carroll and Knauss (2005) and involved a static titanium solution reactor connected by a pulseless dual-cylinder pump to a constantly stirred titanium mixed-flow reactor (Fig. 1). Within the mixed-flow reactor, influent solution was forced to circulate upwards past chlorite grains held between fine titanium mesh in an isolated cylindrical chamber before reaching the reactor outlet, thus ensuring liquid-chlorite contact under continuously mixed conditions. System pressure was controlled at the outlet by a dome-loaded back-pressure regulator. All wetted surfaces (including pump cylinders and back-pressure regulator) were either C-276 alloy or passivated titanium. Maintaining the static vessel temperature above the experimental reactor temperature and allowing CO_2-equilibrated solutions to cool during pressurized passage through the dual-cylinder pump ensured that $CO_{2(aq)}$ stayed in solution as a result of retrograde solubility.

Experiments were initiated by vacuum-evacuating the system between the dual-cylinder pump and the three-way valve/vacuum
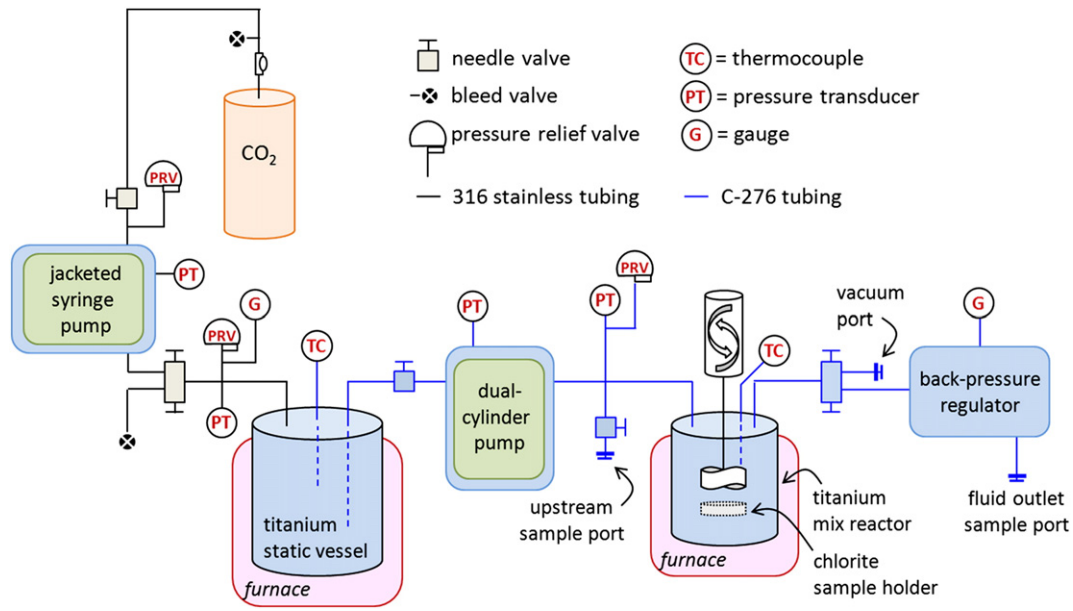
Fig. 1. Schematic of experimental mixed-flow reactor system. PRV indicates pressure relief valve.

port (Fig. 1), pumping 85 °C *CO₂-free* 0.05 m NaCl solution from the static vessel into the mixed-flow reactor until pressurized to the desired level, and then valving off the reactor from the static brine vessel. The static vessel was then pressurized with gaseous or liquid CO_2

and heated to the necessary temperature to achieve desired $CO_{2(aq)}$ concentrations in the solution, generally overnight. After the CO_2 equilibration period, the mixed-flow reactor was quickly brought to the desired experimental temperature. At that point, CO_2-equilibrated

Table 1
Chlorite experimental conditions and measured dissolution rates in both CO_2-equilibrated and CO_2-free solutions.

Expt ID	T (°C)	$CO_{2(aq)}$ (M)	pH[a]	Dissolution rate (mol chlorite m^{-2} s^{-1})	
				Si-derived	Mg-derived
CO_2-acidified experiments ("C")					
C1	275	0.195	4.80	2.41 ($\pm$0.25) $\cdot$ 10^{-11}	2.20 ($\pm$0.23) $\cdot$ 10^{-11}
C2	275	0.20	4.81	2.93 ($\pm$0.31) $\cdot$ 10^{-11}	2.64 ($\pm$0.27) $\cdot$ 10^{-11}
C5	250	0.10	4.84	2.33 ($\pm$0.25) $\cdot$ 10^{-11}	2.53 ($\pm$0.27) $\cdot$ 10^{-11}
C3	250	0.19	4.67	3.71 ($\pm$0.39) $\cdot$ 10^{-11}	3.45 ($\pm$0.35) $\cdot$ 10^{-11}
C3 (rep)	250	0.20	4.58	4.04 ($\pm$0.44) $\cdot$ 10^{-11}	2.77 ($\pm$0.32) $\cdot$ 10^{-11}
C9[b]	200	0.12	4.54	7.57 ($\pm$0.84) $\cdot$ 10^{-11}	4.30 ($\pm$0.48) $\cdot$ 10^{-11}
C9 (rep)	200	0.12	4.54	6.22 ($\pm$0.67) $\cdot$ 10^{-11}	5.21 ($\pm$0.53) $\cdot$ 10^{-11}
C6	200	0.20	4.38	8.70 ($\pm$0.91) $\cdot$ 10^{-11}	6.79 ($\pm$0.70) $\cdot$ 10^{-11}
C7	200	0.36	4.05	4.45 ($\pm$0.46) $\cdot$ 10^{-11}	4.42 ($\pm$0.52) $\cdot$ 10^{-11}
C10	200	0.52	4.06	9.35 ($\pm$1.0) $\cdot$ 10^{-11}	7.49 ($\pm$0.99) $\cdot$ 10^{-11}
C12	150	0.11	3.93	1.90 ($\pm$0.20) $\cdot$ 10^{-11}	1.66 ($\pm$0.17) $\cdot$ 10^{-11}
C13	150	0.19	3.85	3.04 ($\pm$0.33) $\cdot$ 10^{-11}	2.72 ($\pm$0.34) $\cdot$ 10^{-11}
C19	150	0.30	3.72	2.43 ($\pm$0.26) $\cdot$ 10^{-11}	2.09 ($\pm$0.22) $\cdot$ 10^{-11}
C8	150	0.39	3.60	1.04 ($\pm$0.11) $\cdot$ 10^{-11}	9.45 ($\pm$0.97) $\cdot$ 10^{-12}
C11	150	0.51	3.56	1.67 ($\pm$0.19) $\cdot$ 10^{-11}	1.34 ($\pm$0.18) $\cdot$ 10^{-11}
C16	100	0.11	3.70	6.60 ($\pm$0.69) $\cdot$ 10^{-12}	4.04 ($\pm$0.41) $\cdot$ 10^{-12}
C14	100	0.20	3.57	6.84 ($\pm$0.73) $\cdot$ 10^{-12}	5.76 ($\pm$0.59) $\cdot$ 10^{-12}
C15	100	0.30	3.49	1.11 ($\pm$0.12) $\cdot$ 10^{-11}	8.91 ($\pm$1.4) $\cdot$ 10^{-12}
C18	100	0.53	3.35	7.50 ($\pm$0.79) $\cdot$ 10^{-12}	5.43 ($\pm$0.84) $\cdot$ 10^{-12}
CO_2-free/HCl experiments ("H")					
H1-A	100	n.a.	3.01/3.02	1.86 ($\pm$0.25) $\cdot$ 10^{-11}	1.91 ($\pm$0.22) $\cdot$ 10^{-11}
H1-B	100	n.a.	4.05/4.16	3.19 ($\pm$0.34) $\cdot$ 10^{-12}	3.21 ($\pm$0.35) $\cdot$ 10^{-12}
H1-C	100	n.a.	5.00/5.69	3.74 ($\pm$0.40) $\cdot$ 10^{-12}	4.08 ($\pm$0.49) $\cdot$ 10^{-12}
H2-A	200	n.a.	3.00/3.63	1.07 ($\pm$0.12) $\cdot$ 10^{-10}	1.34 ($\pm$0.15) $\cdot$ 10^{-10}
H2-A (rep)	200	n.a.	2.98/3.34	1.25 ($\pm$0.14) $\cdot$ 10^{-10}	1.64 ($\pm$0.20) $\cdot$ 10^{-10}
H2-B	200	n.a.	4.01/4.55	5.71 ($\pm$0.61) $\cdot$ 10^{-12}	5.95 ($\pm$0.72) $\cdot$ 10^{-12}
H2-C	200	n.a.	5.04/4.33	8.07 ($\pm$0.87) $\cdot$ 10^{-12}	7.79 ($\pm$1.0) $\cdot$ 10^{-12}
H3-A	275	n.a.	3.00/4.41	1.53 ($\pm$0.16) $\cdot$ 10^{-10}	1.62 ($\pm$0.18) $\cdot$ 10^{-10}
H3-B[c]	275	n.a.	4.00/5.32	1.64 ($\pm$0.17) $\cdot$ 10^{-11}	1.56 ($\pm$0.17) $\cdot$ 10^{-11}
H3-C	275	n.a.	6.13/5.40	6.45 ($\pm$0.69) $\cdot$ 10^{-12}	2.44 ($\pm$0.27) $\cdot$ 10^{-12}

[a] Listed pH is average modeled value during steady-state times for "C" experiments; for "H" experiments, first value is initial solution pH and second value is modeled steady-state pH (T).
[b] Experiment conducted under unstirred conditions due to stirrer malfunction.
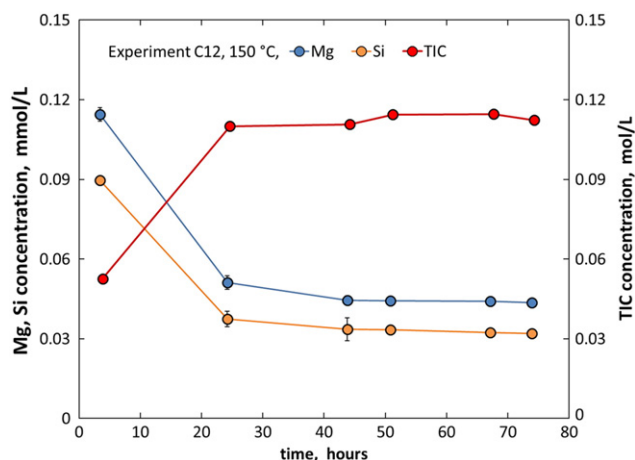[c] Experiment terminated early ($T = 49.5$ h) due to back-pressure regulator malfunction.

Fig. 2. Chlorite dissolution at 150 °C, showing Si, Mg, and total inorganic carbon (TIC) concentrations as a function of time.

solution, siphoned from the bottom of the static vessel, was introduced to the mixed-flow reactor and pumped through the system at a constant 0.5 mL/min rate for 72 h. Pump flowrates were gravimetrically confirmed during each sample collection.

2.3. Sample collection and chemical data treatment

Samples were collected directly downstream of the back-pressure regulator through a luer-lock port. Total inorganic carbon (TIC) samples were collected by attaching a syringe (pre-filled with 1 N NaOH) directly to the port and allowing the sample to degas into the solution where it was "trapped" as dissolved carbonate until analysis via automated carbon analyzer. Degassed samples were collected, filtered (0.2 μm) and acidified, and analyzed for Si, Mg, Al, Fe, Ca, and other trace metals by inductively-coupled plasma mass spectrometry. Because analytical errors in silica, magnesium, aluminum, and iron were small compared to absolute concentrations, uncertainty in these values is considered two times the standard deviation among samples collected during steady-state periods. Experimental system "blank" tests revealed elevated background contributions of iron,
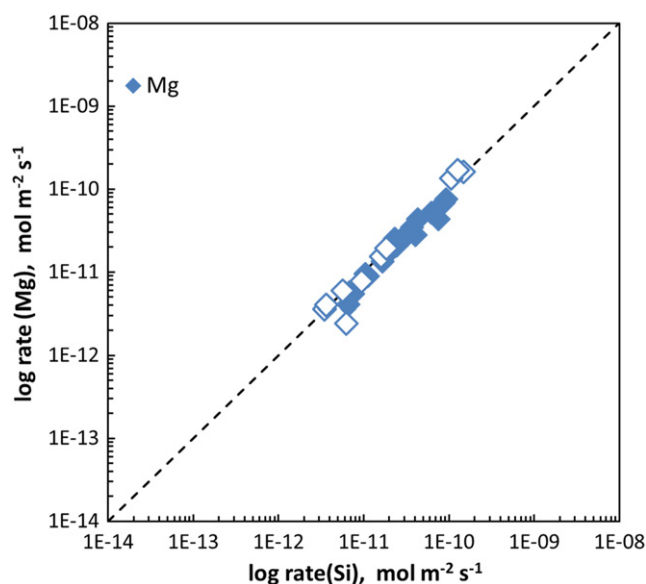

Fig. 3. Comparison of magnesium versus silica release rate. Filled symbols denote experiments with $CO_{2(aq)}$; open symbols denote CO_2-free (control) experiments; dashed line indicates 1:1 relationship. All release rates are normalized to cation abundance in chlorite structure. Errors in rate measurement are commensurate with size of data.

presumably from the high-temperature degradation of components within the magnetic stirrer apparatus. This experimental artifact, coupled with the low initial iron composition of the chlorite material, forced us to exclude iron-derived rate values from further consideration. Chloride concentrations were analyzed by ion chromatography to monitor for possible changes to solution ionic strength (none noted). During CO_2-free experiments, unfiltered degassed samples were also measured for pH after cooling to room temperature.

The geochemical code Geochemist's Workbench (GWB; Bethke and Yeakel, 2010) and *thermo.dat* database were used to calculate aqueous speciation, solution pH, and Gibbs free energies of reaction. The solution pH of CO_2-containing experiments was modeled by first charge-balancing chemical analyses on chloride at 25 °C, adding the measured TIC value as bicarbonate, and then bringing the solution data to run temperature while charge-balancing on hydrogen. CO_2-free experiments and measured 25 °C solution pH values were temperature-corrected by charge-balancing on chloride and bringing to run temperatures.

3. Results and discussion

In this paper we discuss the congruency of observed chlorite dissolution, the absence of any secondary mineral precipitates or effect of $CO_{2(aq)}$ concentrations, and derive an applicable rate equation to describe chlorite dissolution as a function of temperature and acidity. Individual element-specific dissolution rates were stoichiometrically normalized to moles of chlorite mineral and are listed in Table 1.

3.1. Congruency of chlorite dissolution

Over a temperature range of 100–275 °C, we observed near-stoichiometric release of magnesium with respect to silica for both $CO_{2(aq)}$ and CO_2-free experiments (Fig. 3), while iron and aluminum were released in highly non-stoichiometric quantities (Fig. 4). Based on the comparison of Figs. 3 and 4, we conclude that silica and magnesium provide reliable measures of chlorite dissolution rate magnitude and thus we use only rate values derived from these elements in all further discussion. Previous 25 °C studies have noted both incongruent and congruent steady-state chlorite dissolution with respect to silica concentrations, with no consistent trends in relation to pH when all studies are considered as a whole (Ross, 1967; Brandt et al., 2003; Gustafsson and Puigdomenech, 2003; Hamer et al., 2003; Lowson et al., 2005; Malmstrom et al., 2005).

Aluminum and iron release rates vary widely in comparison to silica (Fig. 4). Such non-stoichiometric behavior may have resulted from contamination by iron-bearing parts of the experimental set-up, a possible dependence of rate on aluminum concentrations, or secondary mineral precipitation. Elevated levels of iron (in comparison to expected minimal concentrations due to the low-Fe content of the chlorite) detected during sample-free blank experiments complicated further interpretation of the iron release data. A weak correlation ($R^2 \approx 0.3$) between a^3_H/a_{Al} (hydrogen and aluminum solution activities) and the dissolution rate may suggest that chlorite dissolution depends on dissolved aluminum, as proposed for other silicate minerals by Oelkers et al. (1994) and modeled for chlorite at 25–95 °C by Lowson et al. (2007). However, we did not collect rate data over a wider range of dissolved aluminum conditions to develop a rate law accounting for this type of dependence.

3.2. Lack of secondary precipitation

The precipitation of a secondary phase (especially one containing silica) as a result of chlorite reaction would have affected the elemental release rates measured in our experiments, leading to underestimates of true chlorite dissolution rates. Accordingly, we employed several techniques to detect the presence of secondary reaction
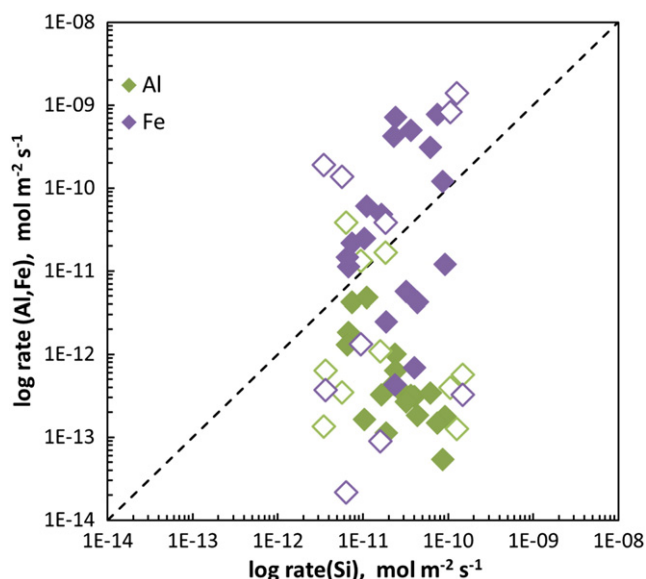
Fig. 4. Comparison of aluminum and iron versus silica release rate. Filled symbols denote experiments with $CO_{2(aq)}$; open symbols denote CO_2-free (control) experiments; dashed line indicates 1:1 relationship. All release rates are normalized to cation abundance in chlorite structure. Errors in rate measurement are commensurate with size of data.

product phases. XRD diffraction patterns collected on reacted solid grains from experiments C18 and C1 (100 and 275 °C, Table 1) showed no evidence for detectable volumes of any new mineral phases. Additionally, chlorite reaction at 200 °C and 10 MPa pCO_2 within a specially constructed microcell showed no detectable change in in situ XRD pattern (H.T. Schaef, Pacific Northwest National Laboratory, personal communication). Solid grains from experiment C1 were also inspected by SEM, with subsampled sections subjected to transmission electron microscopy (TEM); high-resolution electron dispersive spectroscopy detected no new phases or significant differences between C1 material and unreacted chlorite samples. Finally, the potential for amorphous silica phase precipitation was investigated via analysis of C1 reacted material via cross-polarization magic angle spinning NMR. The single ^{29}Si peak in the collected spectra was within the range previously observed for clinochlore chlorite samples (Welch et al., 1995). No additional peaks arising from additional silica-containing minerals were observed, even under experimental conditions chosen specifically to probe for the
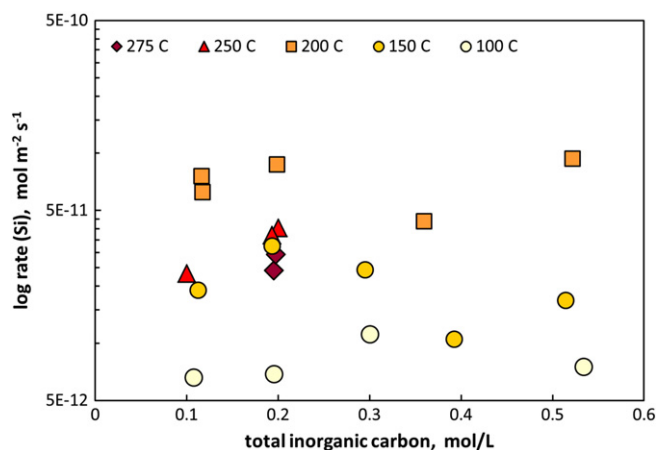
Fig. 5. Log silica-derived chlorite dissolution rates versus total inorganic carbon (including $CO_{2(aq)}$) concentration. Experimental temperature indicated by datum color, from 100 to 275 °C. Errors in rate measurement are commensurate with size of data. (For interpretation of the references to color in this figure legend, the reader is referred to the web version of this contribution.)
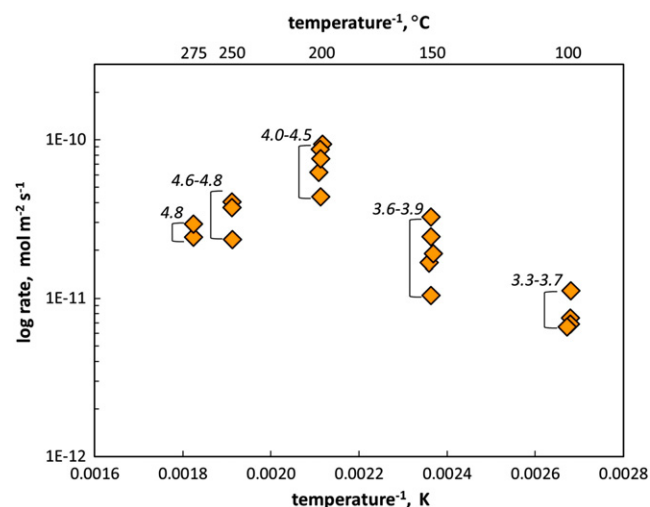
Fig. 6. Log chlorite dissolution rates versus inverse temperature for experiments containing $CO_{2(aq)}$. Adjacent brackets indicate pH range over which data were collected.

presence of proton-rich amorphous silica phases (e.g., Liu and Maciel, 1996).

3.3. Combined effects of dissolved CO_2, temperature, and pH

Chlorite dissolution rates were measured in solutions spanning 0.1–0.5 mol L^{-1} TIC at 100, 150, and 200 °C, and 0.1–0.2 mol L^{-1} TIC at higher temperatures due to pressure vessel limitations. Measured rates range from $6.4 \cdot 10^{-12}$ to $7.9 \cdot 10^{-11}$ mol m^{-2} s^{-1} (Fig. 5), and remained relatively constant as a function of dissolved CO_2 at constant temperature, showing no effect of varying $CO_{2(aq)}$ concentrations (measured as total inorganic carbon). Temperature appears to have a stronger effect on dissolution than does the concentration of dissolved CO_2.

Fig. 6 shows chlorite dissolution data for all experiments containing introduced $CO_{2(aq)}$ as a function of inverse temperature. A maximum dissolution rate was observed at 200 °C, with dissolution rates falling off at temperatures above and below this value. This "turnover" in reaction rate is due to the combined effects of both temperature and pH. Generally, silicate mineral dissolution rates increase with temperature and acidity. In our CO_2-containing experiments, the actual acidity depends upon the dissociation of water and $CO_{2(aq)}$, both of which are temperature-dependent reactions (Fig. 7):

$$H_2O_{(1)} \leftrightarrow H^+ + OH^- \qquad (2)$$

and

$$CO_{2(aq)} + H_2O \leftrightarrow H^+ + HCO_3^-. \qquad (3)$$

As temperatures increase up to 200 °C, the dissociation constant of water increases by approximately 2.5 orders of magnitude and neutral water pH accordingly decreases from 7 to 5.7. From 200 to 300 °C the dissociation constant is predicted to be largely independent of temperature. Conversely, the reaction of $CO_{2(aq)} \rightarrow HCO_3^-$ becomes less and less favored at higher temperatures, effectively releasing fewer hydronium atoms into solution per mole of dissolved CO_2. Chlorite dissolution rates increase from 100 to 200 °C because the effect of temperature is greater than that of solution pH (for 3.3 < pH < 4.5). The rates decrease from 200 to 275 °C because the same concentration of dissolved CO_2 produces a less acidic solution, lessening the potential for chlorite dissolution. At these higher temperatures, rate increases due to temperature are partially offset by rate decreases due to less acidic solutions (4.0 < pH < 4.8).
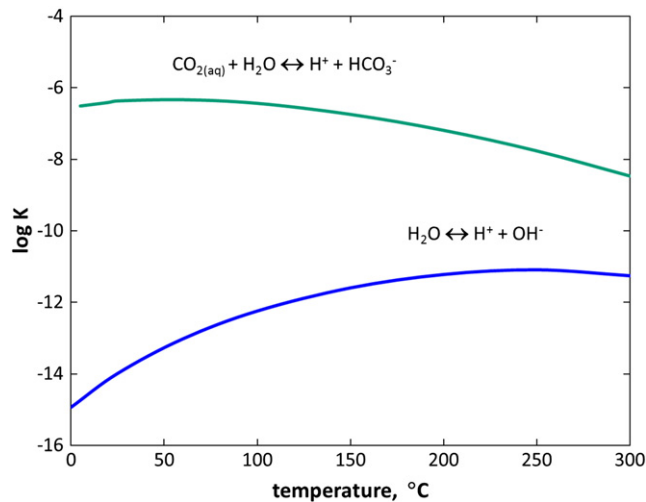
Fig. 7. Log K constants as a function of temperature, for Eqs. (2) and (3), according to thermo.dat database. Note that neutral pH is determined as 0.5(log K_{water}).
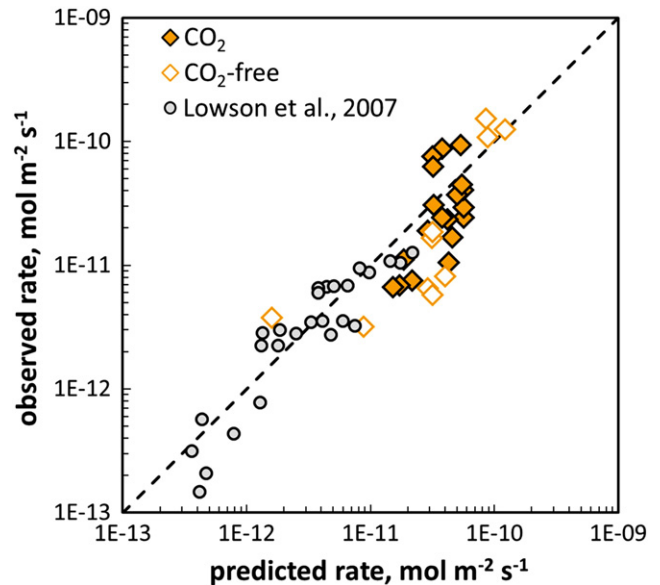

Fig. 8. Observed versus predicted dissolution rates for data from this study as well as selected data from Lowson et al. (2007) (pH 3–5).

3.4. Derivation of dissolution rate equation

Far from equilibrium, chlorite dissolution rate behavior (normalized by surface area) from 100 to 275 °C, pH 3.3–5.7, and $CO_{2(aq)}$ from 0 to 0.5 m can be described with an H^+-catalyzed dissolution mechanism:

$$rate = k_{acid,298\,K} \cdot \exp\left[\left(\frac{-E_{acid}}{R}\right) \cdot \left(\frac{1}{T} - \frac{1}{298\,K}\right)\right] \cdot a_{H+}^n,\qquad(4)$$

where $k_{acid,298\,K}$ and E_{acid} represent the 25 °C kinetic rate constant and activation energy for the acid dissolution mechanism, R is the universal gas constant, T is temperature in Kelvin, a_i denotes the aqueous activity of species i (here, H^+), and n is the order of reaction with respect to proton activity. Optimized parameter values are log $k_{acid,298\,K} = -9.91$ mol m^{-2} s^{-1}, $E_{acid} = 25.1$ kJ mol^{-1}, and $n = 0.488$. The derived rate expression should be tractable for incorporation into numerical simulations after addition of a reaction affinity term, as it is similar in form to many published kinetic rate expressions already handled by reactive transport codes.

In an effort to produce a meaningful rate equation (Eq. 4) we adopted the following protocol. Rate data collected in this study were normalized to a unit specific surface area value, and then optimized values of E_{acid}, the pre-exponential factor A_{acid}, and n were obtained from an unweighted least-squares linear regression of the rate data to Eq. (5):

$$lograte = \log(A_{acid}) - \left(\frac{E_{acid}}{2.303 \cdot R \cdot T}\right) - (n \cdot pH).\qquad(5)$$

Regressions were performed using the data collected in this study, and also with an expanded dataset that included selected 25–95 °C rate data falling within the same pH range from Lowson et al. (2007). The lower-temperature Lowson et al. (2007) data were obtained from similar single-pass flow-through experiments, conducted on a smaller size fraction of a more iron-rich chlorite specimen (Lowson et al., 2005, 2007). Nevertheless, at 95–100 °C, both datasets overlapped and showed excellent agreement at that temperature range. The order of parameter fitting was varied and the best fits (as determined by the coefficient of determination, R^2) were obtained by using the largest dataset (that including the values of Lowson et al., 2007) and optimizing E_{acid} first, then n, and finally A_{acid}. The agreement between observed and predicted rates is shown in Fig. 8 for CO_2-containing and CO_2-free data collected in this study as well as for selected Lowson et al. (2007) data used to better constrain rate parameter values. It should be noted that the activation energy valued derived here, $E_{acid} = 25.1$ kJ mol^{-1},

is more than three times lower than the 80 kJ mol^{-1} value given for both acid and neutral pH rate mechanisms in Palandri and Kharaka (2004; derived from Nagy's (1995) treatment of chlorite data originally collected by Ross (1967)), implying a much lower dependence of dissolution rate on temperature than previously thought. The value of n derived here is equal to that found by Lowson et al. (2005) at 25 °C, and is similar to the values of 0.3–0.6 from other 25 °C chlorite studies (Brandt et al., 2003; Gustafsson and Puigdomenech, 2003). Finally, the 25 °C rate constant value determined here, log $k_{acid,298\,K} = -9.91$ (from log $A_{acid} = -5.51$), is slightly lower than that given by Lowson et al. (2005; log $k_{acid} = -9.79$) but several orders of magnitude higher than that predicted by the general hydrothermal silicate relationship proposed by Wood and Walther (1983).

4. Summary

The objective of this suite of experiments was to measure chlorite mineral dissolution kinetics at temperatures above 100 °C, representative of subsurface temperatures in reservoirs considered for enhanced geothermal development or for deep geologic carbon sequestration or nuclear waste disposal (i.e., higher temperature settings), and to describe this dissolution in the form of a kinetic rate equation. The resulting rate equation is dependent on temperature and pH, but independent of pCO_2, because we did not observe significant differences in dissolution rate attributable to elevated CO_2 beyond decreases in solution pH. We propose this rate equation to describe Mg-rich chlorite dissolution under far-from-equilibrium conditions as a function of pH (under slightly acidic to near-neutral conditions, pH 3.0–5.7) and temperature (up to 275 °C). The rate equation invokes only an acid (pH-dependent) mechanism to describe data collected under the constrained CO_2 solubility/pH conditions in this study. The derived rate expression can be easily incorporated into most reactive transport codes for numerical simulations.

While this study has supplied data to fill one of many gaps in the geochemical literature, it also provides strong caution against extrapolation of other low-temperature silicate mineral rate data to geothermal temperatures. In most cases extrapolations are undertaken out of necessity due to lack of data at temperatures of interest. The most relevant finding from this work is that chlorite dissolution rates do not increase as strongly with temperature (Fig. 9) as has been predicted from extrapolation of lower-temperature kinetic
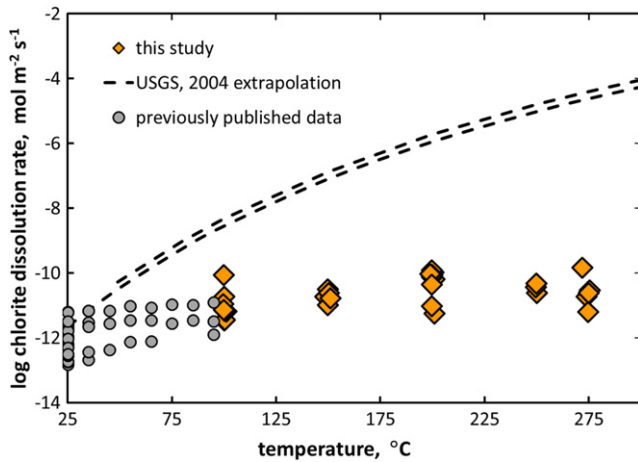
Fig. 9. Log chlorite dissolution rates versus temperature, with extrapolation of kinetic rate published in Palandri and Kharaka (2004) over pH range 3–5 shown as dashed lines. Previously published data over the same pH range from Gustafsson and Puigdomenech (2003), Hamer et al. (2003), Kameda et al. (2009), Lowson et al. (2005, 2007), and May et al. (1995).

studies. The large discrepancy between measured and predicted rates results from an activation energy which is roughly one-third of that reported by Palandri and Kharaka (2004).

Another important finding of this work is that elevated concentrations of dissolved CO_2 representative of CO_2-EGS or geologic carbon storage enhance chlorite dissolution only indirectly, by increasing the acidity of the aqueous phase. No other effects on chlorite dissolution rate were observed as a function of $CO_{2(aq)}$ concentration. For CO_2-rich geothermal or CO_2-EGS systems, the combined effects of decreasing CO_2 solubility as well as the dissociation of $CO_{2(aq)}$ and H_2O should yield lower dissolution rates above 200 °C because the resulting solutions are closer to neutral (less acidic). These same neutral solutions should also lower the acid-catalyzed reactivity of other silicate minerals as well.

For CO_2-EGS operations specifically, these findings imply that the dissolution of chlorite minerals should proceed rather slowly, compared to the framework silicates for which data at comparable temperatures exist (e.g., quartz and albite, log rate values ≈ −11 to −6 over 100–300 °C; Palandri and Kharaka, 2004, and references compiled therein). Lessened reactivity of ubiquitous but rarely high-volume chlorite should result in a correspondingly decreased potential for scaling or alteration products that require Mg, Al, or Si cations for precipitation. While such mineralization reactions may result in additional carbon "trapping" of "lost" injected CO_2 fluids (a proposed net benefit of CO_2-EGS operations), the greater benefit of lessened precipitation and preserved long-term reservoir permeability should outweigh the loss of potential sequestration capability. In addition, this chlorite dissolution rate information can be applied to other higher-temperature (+100 °C) subsurface scenarios, such as enhanced oil recovery and/or carbon sequestration in very deep hydrocarbon or brine reservoirs, or underground nuclear waste disposal.

References

Bethke, C.M., Yeakel, S., 2010. The geochemist's workbench. Release 8.0: Reaction Modeling Guide.University of Illinois, Urbana, Illinois (92 pp.).
Brandt, F., Bosbach, D., Krawczyk-Bärsch, E., Arnold, T., Bernhard, G., 2003. Chlorite dissolution in the acid pH-range: a combined microscopic and macroscopic approach. Geochimica et Cosmochimica Acta 67, 1451–1461. http://dx.doi.org/10.1016/S0016-7037(02)01293-0.
Brown, D.W., 2000. A hot dry rock geothermal energy concept utilizing supercritical CO_2 instead of water. Proceedings, 25th Workshop on Geothermal Reservoir Engineering. Stanford University, Stanford, California (Jan. 24–26, 2000).
Carroll, S.A., Knauss, K.G., 2005. Dependence of labradorite dissolution kinetics on $CO_{2(aq)}$, $Al_{(aq)}$, and temperature. Chemical Geology 217, 213–225. http://dx.doi.org/10.1016/j.chemgeo.2004.12.008.
Dove, P.M., Crerar, D.A., 1990. Kinetics of quartz dissolution in electrolyte solutions using a hydrothermal mixed flow reactor. Geochimica et Cosmochimica Acta 54, 955–969. http://dx.doi.org/10.1016/0016-7037(90)90431-J.
Duan, A., Sun, R., Zhu, C., Chou, I., 2006. An improved model for the calculation of CO_2 solubility in aqueous solutions containing Na^+, K^+, Ca^{2+}, Mg^{2+}, Cl^-, and SO_4^{2-}. Marine Chemistry 98, 131–139. http://dx.doi.org/10.1016/j.marchem.2005.09.001.
Foster, M.D., 1962. Interpretation of the composition and a classification of the chlorites. Geological Survey Professional Paper 414-A.U.S. Geological Survey, Washington, D.C (38 pp.).
Garcia, D.J., Shao, H., Hu, Y., Jun, Y., 2012. Supercritical CO_2-brine induced dissolution, swelling, and secondary mineral formation on phlogopite surfaces at 75–95 °C and 75 atm. Energy & Environmental Science 5, 5758–5767. http://dx.doi.org/10.1039/c2ee02026b.
Gaus, I., Audigane, P., André, L., Lions, J., Jacquemet, N., Durst, P., Czernichowski-Lauriol, I., Azaroual, M., 2008. Geochemical and solute transport modelling for CO_2 storage, what to expect from it? International Journal of Greenhouse Gas Control 2, 605–625. http://dx.doi.org/10.1016/j.ijggc.2008.02.011.
Gustafsson, A.B., Puigdomenech, I., 2003. The effect of pH on chlorite dissolution rates at 25 °C. Materials Research Society Symposium Proceedings 757, 649–655. http://dx.doi.org/10.1557/PROC-757-II3.16.
Hamer, M., Graham, R.C., Amrhein, C., Bozhilov, K.N., 2003. Dissolution of ripidolite (Mg, Fe-chlorite) in organic and inorganic acid solutions. Soil Science Society of America Journal 67, 654–661. http://dx.doi.org/10.2136/sssaj2003.6540.
Hu, Y., Jun, Y., 2012. Biotite dissolution in brine at varied temperatures and CO_2 pressures: its activation energy and potential CO_2 intercalation. Langmuir 28, 14633–14641. http://dx.doi.org/10.1021/la3028995.
Kameda, J., Sugimori, H., Murakami, T., 2009. Modification to the crystal structure of chlorite during early stages of its dissolution. Physics and Chemistry of Minerals 36, 537–5445. http://dx.doi.org/10.1007/s00269-009-0299-x.
Li, L., Peters, C.A., Celia, M.A., 2006. Upscaling geochemical reaction rates using pore-scale network modeling. Advances in Water Resources 29, 1351–1370. http://dx.doi.org/10.1016/j.advwatres.2005.10.011.
Liu, C.H.C., Maciel, G.E., 1996. The fumed silica surface: a study by NMR. Journal of the American Chemical Society 118, 5103–5119.
Lowson, R.T., Comarmond, M.C.J., Rajaratnam, G., Brown, P.L., 2005. The kinetics of the dissolution of chlorite as a function of pH and at 25 °C. Geochimica et Cosmochimica Acta 69, 1687–1699. http://dx.doi.org/10.1016/j.gca.2004.09.028.
Lowson, R.T., Brown, P.L., Comarmond, M.C.J., Rajaratnam, G., 2007. The kinetics of chlorite dissolution. Geochimica et Cosmochimica Acta 71, 1431–1447. http://dx.doi.org/10.1016/j.gca.2006.12.008.
Lu, J., Kharaka, Y.K., Thordsen, J.J., Horita, J., Karamalidis, A., Griffith, C., Hakala, J.A., Ambats, G., Cole, D.R., Phelps, T.J., Manning, M.A., Cook, P.J., Hovorka, S.D., 2012. CO_2-rock–brine interactions in Lower Tuscaloosa formation at Cranfield CO_2

sequestration site, Mississippi, U.S.A. Chemical Geology 291, 269–277. http://dx.doi.org/10.1016/j.chemgeo.2011.10.020.

Maher, K., Steefel, C.I., DePaolo, D.J., Viani, B.E., 2006. The mineral dissolution rate conundrum: insights from reactive transport modeling of U isotopes and pore fluid chemistry in marine sediments. Geochimica et Cosmochimica Acta 70, 337–363. http://dx.doi.org/10.1016/j.gca.2005.09.001.

Malmstrom, M., Banwart, S., Lewerhagen, J., Duro, L., Bruno, J., 2005. The dissolution of biotite and chlorite at 25 °C in the near-neutral pH region. Journal of Contaminant Hydrology 21, 201–213. http://dx.doi.org/10.1016/S0148-9062(97)87367-6.

May, H.M., Acker, J.G., Smyth, J.R., Bricker, O.P., Dyar, M.D., 1995. Aqueous dissolution of low-iron chlorite in dilute acid solutions at 25 °C. Clay Minerals Society, Program and Abstracts 32, 8819.

Nagy, K.L., 1995. Dissolution and precipitation kinetics of sheet silicates. In: White, A.F., Brantley, S.L. (Eds.), Chemical Weathering Rates of Silicate Minerals. Mineralogical Society of America, Washington, D.C, pp. 173–233.

Oelkers, E.H., Schott, J., Devidal, J., 1994. The effect of aluminum, pH, and chemical affinity on the rates of aluminosilicate dissolution reactions. Geochimica et Cosmochimica Acta 58, 2011–2024. http://dx.doi.org/10.1016/0016-7037(94)90281-X.

Palandri, J.L., Kharaka, Y.K., 2004. A compilation of rate parameters of water–mineral interaction kinetics for application to geochemical modeling. U.S. Geological Survey Open File Report 2004-1068 (70 pp.).

Post, J.L., Plummer, C.C., 1972. The chlorite series of Flagstaff Hill area, California: a preliminary investigation. Clays and Clay Minerals 20, 271–283.

Pruess, K., 2006. Enhanced geothermal systems (EGS) using CO_2 as a working fluid — a novel approach for generating renewable energy with simultaneous sequestration of carbon. Geothermics 35, 351–367. http://dx.doi.org/10.1016/j.geothermics.2006.08.002.

Ross, G.J., 1967. Kinetics of acid dissolution of an orthochlorite mineral. Canadian Journal of Chemistry 45, 3031–3034. http://dx.doi.org/10.1139/v67-491.

Shao, H., Ray, J.R., Jun, Y., 2011. Effects of salinity and the extent of water on supercritical CO_2-induced phlogopite dissolution and secondary mineral formation. Environmental Science & Technology 45, 1737–1743. http://dx.doi.org/10.1021/es1034975.

Tester, J.W., Anderson, B.J., Batchelor, A.S., Blackwell, D.D., DiPippo, R., Drake, E.M., Garnish, J., Livesay, B., Moore, M.C., Nichols, K., Petty, S., Toks z, M.N., Veatch, R.W., Baria, R., Augustine, C., Murphy, E., Negraru, P., Richards, M., 2006. The Future of Geothermal Energy: Impact of Enhanced Geothermal Systems (EGS) on the United States in the 21st Century. Massachusetts Institute of Technology (DOE Contract DE-AC07-05ID14517, 372 pp.).

Welch, M.D., Barras, J., Klinowski, J., 1995. A multinuclear NMR study of clinochlore. American Mineralogist 80, 441–447.

Wolery, T.J., Carroll, S.A., 2010. CO_2–rock interactions in EGS-CO_2: New Zealand TVZ geothermal systems as a natural analog. GRC Transactions 34, 729–736.

Wood, B.J., Walther, J.V., 1983. Rates of hydrothermal reactions. Science 222, 413–415.

Xu, T., 2012. Mineral carbonation in a CO_2-EGS geothermal reservoir. Proceedings, 37th Workshop on Geothermal Reservoir Engineering. Stanford University, Stanford, CA (Jan. 30–Feb 1, 2012).